Degradation Mechanism in La$_{0.8}$Sr$_{0.2}$CoO$_3$ as Contact Layer on the Solid Oxide Electrolysis Cell Anode

Vivek Inder Sharma and Bilge Yildiz[*,z]

Laboratory for Electrochemical Interfaces, Department of Nuclear Science and Engineering, Massachusetts Institute of Technology, Cambridge, Massachusetts 02139, USA

Detailed chemical and structural analyses are presented for the degradation mechanism of La$_{0.8}$Sr$_{0.2}$CoO$_3$ (LSC) as the contact layer of solid oxide electrolysis cell (SOEC) anodes. SOEC stack cells, which were operated in the presence of Cr-containing interconnects, and reference half-cells, which were tested with Pt interconnects, were investigated. The as-prepared surface chemistry of LSC showed a spatially uniform A-site (La and Sr) enrichment. Undesirable secondary phases of Cr$_2$O$_3$, LaCrO$_3$, La$_2$CrO$_6$, and Co$_3$O$_4$ were identified in the contact layer of the SOEC stack cells, which had significantly reduced electrochemical performance after long-term testing. Auger electron spectroscopy and analytical transmission electron microscopy showed the presence of Cr throughout the layer cross section on the surface and in the bulk, respectively, with significant variations in the local chemistry at the micro- to nanoscale. Particularly, a long-range transport of Sr and Co cations out of the LSC phase to the top of the contact layer was evident. However, when tested with electrolytic potential and current without a Cr environment, the LSC contact layer composition remained stable. The dissociation of the LSC in the SOEC stack cells can be, most probably, driven by the La–Cr–O related thermodynamics under the electrolytic potential and oxygen pressure at the anode.
© 2010 The Electrochemical Society.   [DOI: 10.1149/1.3288835] All rights reserved.

High temperature electrolysis is one of the most efficient electrochemical processes to convert electricity and steam or a mixture of steam and CO$_2$ into H$_2$ or syngas (H$_2$ + CO), respectively, using electricity and heat from nuclear plants and concentrated solar plants.[1,2] It is carried out in devices called solid oxide electrolytic cells (SOECs) at high temperatures. High temperature decreases Gibbs' free energy of the reaction and, thus, the electrical energy input required for the electrolysis in comparison to the electrolysis of water at room temperature. However, at the high temperature of operation (above 800°C), a loss in the rate of hydrogen (or syngas) production due to material degradation has been observed. This article investigates the mechanisms of degradation in the contact layer of SOECs, focusing on the diffusion of Cr species from the stainless steel interconnects into the cell structure and the long-range transport and segregation of cations in the contact layer.

The basic principle of operation of SOECs is similar to that of solid oxide fuel cells (SOFCs); the difference being the reverse direction of current. An electrolytic cell consists of the hydrogen electrode (cathode) and the oxygen electrode (anode) with an oxygen ion conducting electrolyte sandwiched between them. For the SOECs investigated in this paper, the hydrogen electrode consists of a Ni–scandia stabilized zirconia (ScSZ) cermet. ScSZ (10% Sc$_2$O$_3$–ZrO$_2$) constitutes the electrolyte. Oxygen electrolyte is composed of a perovskite oxide, A$_{0.8}$Sr$_{0.2}$MnO$_3$ (ASM).[a] Another perovskite oxide, La$_{0.8}$Sr$_{0.2}$CoO$_3$ (LSC), is used as a contact layer between the oxygen electrode and the stainless steel interconnects. Ceramatec Inc. provided SOECs under analysis in this paper after 2000 continuous hours of their operation at 830°C.[3,4]

Degradation Mechanisms: Background

While a high operating temperature increases the efficiency of the SOECs, it also accelerates the degradation rate. This is principally caused by the chemical interactions between the SOEC material constituents, as in SOFCs, resulting in the formation of secondary phases that either block the active electrocatalytic sites or completely transform into inactive local phases.[5] The secondary phases block the reaction and diffusion paths in the perovskite-type electrodes and contact layers, leading to a decrease in their conductivity and electrocatalytic activity. For example, O'Brien et al. measured an 18% loss in H$_2$ production rate over 1000 h of operation of

SOECs.[6] The SOECs investigated in this paper were operated at a constant thermal neutral voltage (1.3 V) at a temperature of 830°C, and the current density (initially at 400 mA/cm^2) decreased by 40% over 2000 h of operation, indicating severe degradation of the cells.[3,4] However, research to date has enabled a better understanding of the SOFC degradation mechanisms and has helped control the degradation rate in SOFC stacks down to lower than 2%/1000 h.[7] On the other hand, a thorough investigation on the governing degradation mechanisms for SOECs is yet at its infancy, with recent attempts to elucidate and control the high degradation rate of the SOECs compared to SOFCs.[8,9] A recent study has presented a silica-related poisoning of the hydrogen/steam electrodes in SOEC, different from that expected in SOFC conditions.[8] This paper focuses on the material degradation on the oxygen electrode side of SOECs.

Cr poisoning of the oxygen electrode,[10-21] segregation of cations to the surface of the catalyst,[22-24] and interdiffusion of cations between the electrolyte and oxygen electrode grains[25] were identified to be crucial processes leading to the degradation of SOFCs. At a high level, SOECs are expected to be subject to similar causes of degradation, which are of interest here. However, the exact mechanisms and the consequent secondary phases could be different from those in an SOFC operation because of the different thermodynamic and electrochemical conditions and the reverse path of ionic and electronic transport in SOECs compared to SOFCs.

The Cr-poisoning of the SOEC materials is the focus of this paper. Therefore, it is worth providing the main messages at this point from the extensively documented studies on the oxygen side (cathode) of SOFCs on the Cr poisoning question[10-21]. Three main hypotheses are found in literature to explain the progression of the Cr-poisoning mechanisms. The first hypothesis suggests that this process is initiated through the formation of Cr^{6+}-containing gaseous species, such as CrO$_3$ or CrO$_2$(OH)$_2$, from the oxidation of chromium oxide on the interconnect.[12,13] The volatile Cr species are then reduced at the triple phase boundaries of electrode, electrolyte, and air and form solid Cr$_2$O$_3$ and other Cr-rich phases, thereby inhibiting the electrochemistry of the electrode and leading to polarization losses.[14,16] For example, the solid Cr$_2$O$_3$ species could react with the perovskite cathode La$_{1-x}$Sr$_x$MnO$_3$ (LSM) to form La$_{1-x}$Sr$_x$Mn$_{1-y}$Cr$_y$O$_3$ and (Cr$_{1-y}$Mn$_y$)O$_{1.5-\delta}$, with the formation of (Cr$_{1-y}$Mn$_y$)O$_{1.5-\delta}$ spinel being the driving force for the reaction.[16] Furthermore, Matsuzaki and Yasuda found that not only the SOFC cathode but also the electrolyte could influence the reduction of the volatile Cr-containing species due to the electrochemical state at the cathode/electrolyte interface.[10] The second hypothesis suggests that, along with the vapor phase reduction, solid-state diffusion of the Cr-containing species into the oxygen electrode and chemical disso-

ciation of the electrode material are underlining mechanisms in the deposition of Cr.[17] Finally, the third and a more recent hypothesis by Zhen et al.[18] and Chen et al.[19] suggests that the Cr deposition process at the oxygen electrode is thermodynamically driven and kinetically limited by a nucleation reaction between the Cr species that is being transported and a "nucleation agent" on the electrode. In the LSM electrode, the nucleation agent was identified to be the manganese species (Mn^{2+}), and for $(La,Sr)(Co,Fe)O_3$ (LSCF) electrode, it was suggested to be the SrO species segregated at the electrode surface.[18] References also assert that the driving force for the deposition of Cr species at the LSM cathode is the generation of Mn^{2+} species, which then react with gaseous Cr species, forming Cr–Mn–O nuclei and, subsequently, the $(Cr,Mn)_3O_4$ spinel. In addition to the electrode, the effects of Cr-related degradation have also been reported for the contact layer of SOFC cathodes. In that case, the formation of a less conducting oxide layer forming between the contact layer and the interconnect was suggested to be responsible for the degradation of the cells due to loss in the electronic path from the interconnect to the cathode.[21] Clearly, there is still no consensus about the exact and global mechanism of how Cr poisons the electrochemical performance of the electrodes due to the complicated dependencies on structure, operating temperature, atmosphere, and ionic and electronic conductivities. Furthermore, the stability of the possible reaction products between Cr and a given oxygen electrode material can differ between the SOFC and SOEC due to the different thermodynamic conditions at the corresponding electrodes.

In addition to Cr poisoning, cation interdiffusion and segregation can adversely affect the performance of the cells through local adverse changes in the composition and structure. The cation interdiffusion between the oxygen electrode and the electrolyte can lead to an electrochemically inferior layer or microstructure formation and has been the subject of detailed studies due to its importance in electrode activity and stability.[22-24] Similar to interdiffusion, but different in location, segregation of cations in the electrodes of SOFCs is well documented.[25] Simner et al. observed that LSCF cathodes, operated for 500 h at 750°C, experience Sr enrichment at the cathode–electrolyte and cathode–current collector interfaces.[25] In this study, the Sr/(La + Sr) ratio increased from 0.4 to 0.9 upon testing and was suggested to account for the increase in both the ohmic and non-ohmic resistances observed for the tested SOFCs. If the extent of such cation interdiffusion and segregation is small, it may not result in drastic changes in the bulk microstructure, and the original bulk phases could be retained, while the adverse effects would be limited to (critical) interfaces where segregation accumulates. However, if the movement and flux of cations is significant over the microstructure, these processes can as well compromise the phase stability and the global electrochemical properties of the cell materials.

Objective

The goal of the research presented in this paper is to identify the governing mechanisms for the loss in the electrochemical performance of the anode (oxygen electrode) contact layer (LSC) leading to the performance degradation of the SOECs. Our specific objective is to identify how the Cr species from the stainless steel interconnects leads to the formation of electrochemically inactive phases dissociated from the LSC contact layer of the tested SOECs. In doing so, consideration of the A-site cation segregation on LSC in the context of Cr reactions is of importance.

Approach

We present the approach used in characterizing the materials' chemistry and structure and the corresponding analyses. We employed spectroscopy and microscopy techniques in an integrated manner, from a high level to a high resolution postmortem analysis. Table I defines the nomenclature for the cells, which are presented in this article. We carried out the analysis on two batches of samples. One batch consisted of the 10 cm × 10 cm full-cell SOECs provided by Ceramatec Inc., both as-prepared and tested (referred to as

Table I. Nomenclature for the cells studied in this paper.

Cell number	Air electrode description
CER#1	As-prepared cell with LSC contact layer on top of the ASM electrode.
CER#2	2000 h tested cell at 830°C with LSC contact layer on top of the ASM electrode.
REF#1	Symmetric half-cell, ASM electrodes with LSC contact layer. Electrochemically ran in air at 820°C for 322 h. Pt mesh in the test, instead of the stainless steel interconnects in CER#2.
REF#2	Symmetric half-cell, ASM electrodes with LSC contact layer. Sintered at 830°C in air for 108 h. No electrochemical treatment.

CER#1 and CER#2, respectively). This batch of samples was investigated to identify the changes in microstructure and chemical composition that were accompanied by their operation in the demonstration tests at Idaho National Laboratory.[3,4] The second batch of samples consisted of reference samples as half-cells that were operated under controlled electrochemical conditions in air. This batch was analyzed to differentiate the mechanism of degradation of an LSC contact layer, as hypothesized, based on the findings from CER#1 and CER#2. These cells, denoted by REF#1 and REF#2, are comprised of ASM as both the anode and the cathode, LSC as the contact layer on both electrodes, and ScSZ as the electrolyte. A schematic of the reference cells is shown in Fig. 1. REF#1 underwent both heat and electrochemical treatment, while REF#2 was subjected to heat-treatment alone. This distinction was made to facilitate the identification of any changes occurring in the microstructure of reference half-cells due to electrochemistry or thermal treatment conditions.

The techniques used and our particular objectives in utilizing each technique are summarized in Fig. 2. The first target of the research was the preliminary identification of the phases present on the top of the LSC contact layer near the interconnect. For this purpose, we performed Raman spectroscopy[26] measurements using a Kaiser Optical Instruments' Halogram 5000 series Raman spectrometer. A laser wavelength of 785 nm and collection fibers providing a spot size of 80 μm were employed. References 27-33 were used to identify the Raman peaks of the phases of interest found in our data.

We investigated the variation in the surface chemistry and microstructure of the LSC contact layer across its cross section and on its top using scanning nanoprobe Auger electron spectroscopy (NAES).[34] NAES was performed using the Physical Electronics model 700 scanning Auger nanoprobe. Incident electrons having an
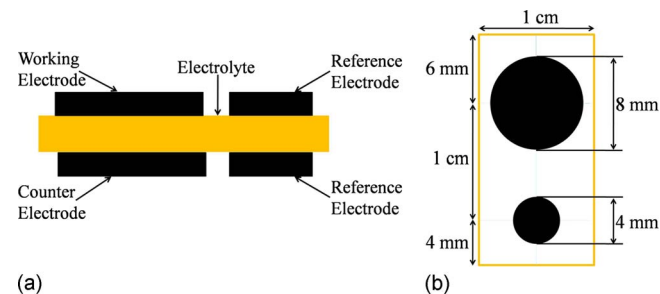

Figure 1. (Color online) Schematic drawing of the reference half-cells in this investigation: (a) cross-sectional view and (b) top view.

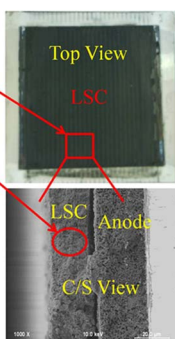| Technique	Objective	
Raman Spectroscopy	Preliminary identification of secondary phases formed on the surface of the bond layer	
Nanoprobe Auger Electron Spectroscopy (NAES)	Electrode surface chemistry and microstructure and its variation across the cross section at a small scale (µm-nm)	
Energy Dispersive X-Ray Spectroscopy (EDX) Transmission Electron Microscopy (TEM)	High resolution identification of the chemical composition and secondary structures formed	
Electrochemical Impedance Spectroscopy	Isolation of LSC dissociation and cation segregation mechanism	

Figure 2. (Color online) Summary of the characterization techniques used and their purpose.

Figure 3. (Color online) Raman spectra from an as-prepared cell, CER#1, compared to a tested cell, CER#2. The formation of secondary phases during the 2000 h test of the cell is evident from the difference in the two spectra with Raman peaks identified for the secondary phases.

energy of 10 keV were used, and smoothing and differentiation of the Auger electron spectroscopy (AES) spectra collected were carried out using the Savitsky–Golay algorithm.

To identify the length scale of the cation segregation and phase dissociation in the bulk of LSC grains at high resolution, transmission electron microscopy (TEM)[35] coupled with energy dispersive X-ray spectroscopy (EDX) was used. This technique complements the findings obtained from the NAES results: TEM/EDX provides information from the bulk of the microstructure, while data in NAES are essentially from the surface. The investigations of the different secondary phases formed at the LSC/interconnect and LSC/ASM interfaces were facilitated by preparing TEM samples from both regions. To prepare the TEM samples, a small portion of the LSC layer was physically lifted from the cells and glued to standard TEM grids made of Cu. The glued sample was then thinned down to electron transparency using a Gatan ion miller, with Ga ions accelerated through a potential of 5 kV. Scanning transmission electron microscopy (STEM) elemental maps were carried out using a JEOL 2010F microscope having a field-emission electron source. The incident electron energy was 200 keV. The EDX microanalysis system, Oxford Instruments INCA, was used for collecting the EDX spectra. The point EDX spectra were acquired with an acquisition time of 300 s and a spot size of 2.4 nm. The quantification of the EDX data was obtained by a standardless analysis using the Cliff–Lorimer correction. For the STEM elemental maps, a JEOL detector was used. A probe of size 0.2 nm with a camera length of 15 cm was employed. The elemental maps were collected within 60–120 s each.

To distinguish the possible causes of long-range cation transport and segregation in the LSC contact layer microstructure, electrochemical tests were conducted on reference half-cells, where Cr and its species were taken out of the system by replacing the stainless steel interconnects used in CER#1 and CER#2 with Pt contact meshes on the LSC layer. To replicate the operating conditions, REF#1 was run in air under a constant current density of 0.40 A/cm^2 (same as the initial current density for CER#1 and CER#2) at 816°C for 13.5 continuous days. We carried out AES and electrochemical impedance spectroscopy (EIS) on the reference cells: on REF#1, after the electrochemical operation and on REF#2, after the thermal treatment without electrochemistry.[b]

Results

A comparison between the Raman spectra from an as-prepared cell (CER#1) and a tested cell (CER#2) is presented in Fig. 3. Raman spectroscopy results showed that the LSC contact layer had
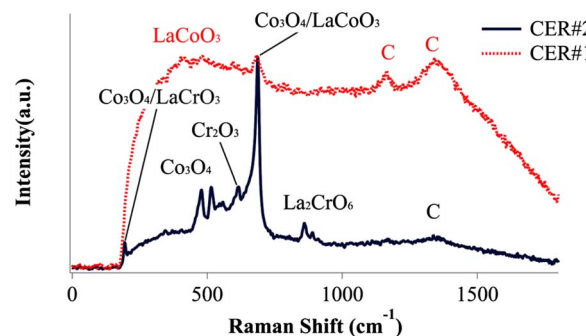
degraded, and the poorly conducting secondary phases were formed. Raman peaks belonging to Cr_2O_3,[27] C,[28] ZrO_2,[29] $LaCrO_3$,[30] La_2CrO_6,[31] $LaCoO_3$,[32] and Co_3O_4[33] were identified from previously published literatures. The comparison between the conductivities, showing 2–6 orders of magnitude decrease in the conductivity of the secondary phases compared to the original LSC contact layer, is summarized in Table II.

Figure 4a is an SEM image from the LSC cross section of CER#2 followed by the AES spectra from the three marked areas in Fig. 4b. AES results show an average Cr fraction (averaged over all the sets of measurements) of approximately 7% (normalized with respect to the sum of La, Co, and Cr content) on the surface of the LSC contact layer grains. Furthermore, the LSC layer exhibited local variation in chemical constituents on the surface of its grains with the La/Co ratio varying from 0.62 to 9.50 for the data shown in Fig. 4. Over all the sets of measurements, the La/Co ratio for CER#2 varied to as high as 16.65. There was no detectable Sr signal, and only a small fraction of Co was identified as remaining on the LSC cross-sectional surface. Contrary to the LSC cross-sectional surface, the AES spectra at the top of LSC (LSC/interconnect interface) showed the presence of Co-rich crystallites and a Sr-rich surface layer, as shown in Fig. 5a. The Co-rich crystallites on the top lack La, whereas the LSC cross section had approximately 70% La (normalized with respect to the sum of La, Co, and Cr content). Sr content in the crystallite-free top region varied from 15–81% with an average of 42% (normalized with respect to the sum of La, Sr, and Cr content). The AES spectra for Co and Sr showing this contrast for the top and the cross section of LSC are presented in Fig. 5b and c.

The dissociation of the LSC contact layer at a scale from a few micrometers to nanometers was studied by STEM elemental mapping on the TEM samples taken from the contact layer both near the anode and the interconnect interfaces. The dark-field TEM images of different regions of a TEM sample prepared from the LSC/interconnect interface region and the elemental maps for La, Sr, Co, and Cr at different length scales are shown in Fig. 6. The point EDX analysis on the samples showed that Cr content in the LSC bulk (normalized with respect to the sum of La, Sr, Co, and Cr content) varied from 10 to 33%. It is evident from Fig. 6 that regions rich in Cr are associated with a high La content and a low Co content and vice versa. Similar to the surface of the LSC grains probed by AES, the LSC bulk was also deficient in Sr with the maximum Sr content in the bulk being 4%. Table III presents the chemical composition of one of the Cr-rich and Co-rich regions found in TEM samples prepared both from the LSC/interconnect and LSC/ASM interfaces. The La/Cr ratio in the bulk was nearly 2 and 1.5 for the regions representative of the LSC/interconnect interface and the LSC/ASM interface, respectively.

The Raman spectroscopy, AES, and TEM results indicate the inhomogeneous dissociation of the LSC contact layer accompanied by the segregation of the cations of LSC. We performed controlled

---

[b] For reference half-cells, because the LSC was sintered in situ, as in stack tests, the AES measurements on them was not possible before their heat-treatment. Therefore, REF#2 serves the purpose of comparing only the electrochemical effects to the thermal effects on LSC.

Table II. Conductivity data for the secondary phases that were identified in the Raman spectra on the tested SOEC anode contact layer.

Constituent	Conductivity (S/cm)	Reference
$La_{0.6}Sr_{0.4}CoO_3$ at 800°C	1.6×10^3	38
$LaCoO_3$ at 900°C	7.6×10^2	39
8 mol % Sc_2O_3–ZrO_2 at 800°C	4.8×10^{-2}	40
Co_3O_4 at 800°C	3.9×10^1	41
Cr_2O_3 at 1000°C	1.0×10^{-3}	42
$LaCrO_3$ at 800°C	3.4×10^{-1}	43

EIS experiments on the reference half-cells, avoiding the presence of Cr in the electrical contacts to isolate the mechanism of cation segregation and LSC dissociation. The performance history curve for REF#1 is shown in Fig. 7. Under a constant applied current density of 0.40 A/cm², the potential difference across the cell increased with time from an initial value of 0.23 V and stabilized at 0.42 V after 4.5 days of operation. Figure 8 compares the Nyquist plot for the anode (electrolytic mode) of REF#1 before and after the operation. The impedance of the anode increased from 0.07 to 0.83 Ω during operation. To identify whether the REF#1 degradation was due to a similar compositional dissociation as in CER#2, we compared the effects of just the thermal treatment without electrochemistry (REF#2) to that of electrochemistry at high temperature (REF#1) on the surface chemical compositions of REF#1 and REF#2. Figure 9 shows AES spectra from an area in each of the anodic contact layer of these two cells. Both REF#1 and REF#2 had similar chemical compositions on the contact layer surface, although the ratio of the A-site to B-site cations is 6.00 and 5.71, respectively, indicating a significant but similar level of segregation of the A-site cations to the surface. To investigate the differences in the CER#2 and REF#1 compositions, we compared their final surface chemistry after the electrochemical tests. The A-site to B-site ratio for REF#1 varied from 5.71–6.71 throughout the AES measurements made across the cross section of its anode-side contact layer. This indicates uniformity and stability of the near-surface compositions in
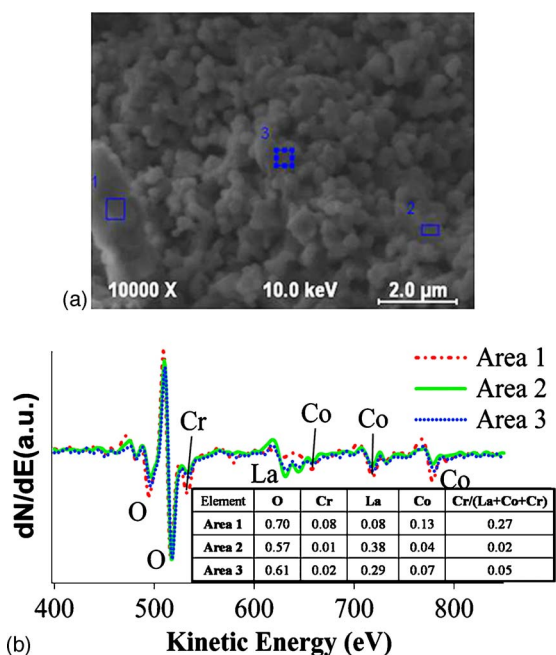
REF#1 as opposed to CER#2. A comparison between the AES spectra from an area in each of the cross section of the anodic contact layer of REF#1 and CER#2 is presented in Fig. 10. The AES peak corresponding to Cr is evident in the spectrum from CER#2 and missing from REF#1, as expected, because CER#2 had stainless steel interconnects.

Discussion

Raman spectroscopy results clearly showed that the LSC contact layer had dissociated into secondary phases having a lower conductivity than the original composition. The presence of Cr-containing phases, Cr_2O_3, $LaCrO_3$, and La_2CrO_6, indicated Cr migration from the stainless steel interconnects into the originally LSC contact layer. The consequent severe decrease in the electronic conductivity of the contact layer, as shown in Table II, suggests that the degradation of the oxygen electrode performance should, in part, be due to the loss in its electronic activation because the contact layer no longer serves for its purpose.

In the SOFC cathode, due to a locally reducing environment, the formation and stability of La_2CrO_6 is not expected. Regarding the thermodynamics of the La–Cr–O system, a recent study of thermodynamic calculations using CALPHAD [36] showed that $LaCrO_3$ is stable up to 1000°C in an atmosphere ranging from pure O_2 to $P_{O_2} = 10^{-16.1}$ Pa. However, La_2CrO_6 forms within a wide temperature range above 700°C at P_{O_2} at and above 10^5 Pa. While the
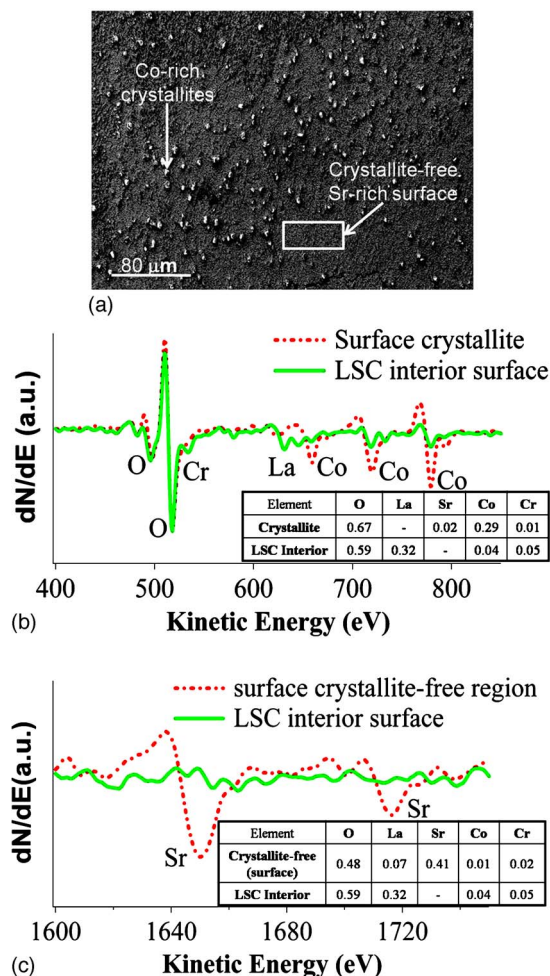

Figure 5. (Color online) (a) SEM image of the top surface of the LSC contact layer cell CER#2, showing Co-rich and Sr-rich phases. AES data from (b) one of the Co-rich crystallites on the top surface of LSC and (c) the Sr-rich surface region free of Co-rich crystallites shown in (a) compared with the AES data from the LSC cross-sectional surface.
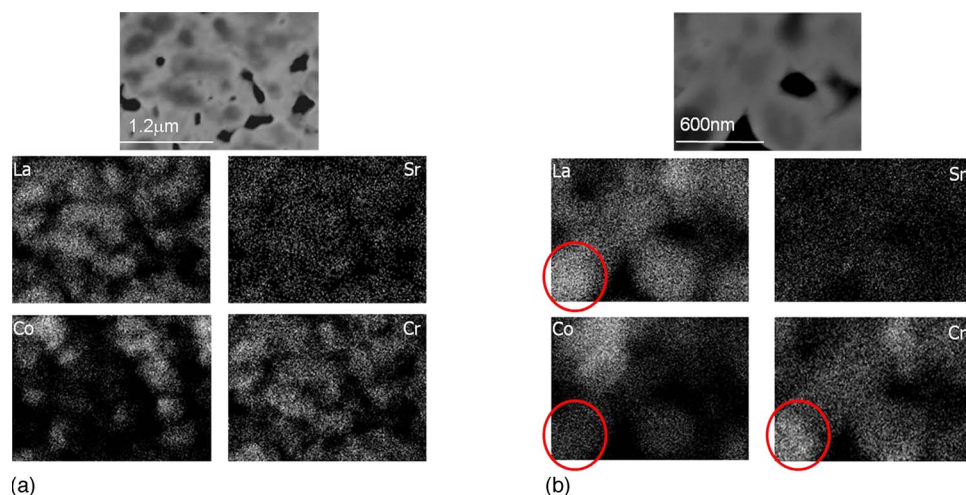

Figure 4. (Color online) (a) SEM image of the cross section of cell CER#2, LSC region. (b) AES data from points 1, 2, and 3 in (a) with fractional content of the constituent elements in the inset table.

Figure 6. (Color online) Dark-field TEM image of a region of the LSC TEM sample with the elemental maps for La, Sr, Co, and Cr (a) at a lower magnification (analysis area: 2.5×1.7 µm) and (b) at a higher magnification (analysis area: 1.3×0.9 µm).

Table III. Chemical composition from the point EDX analysis on the TEM samples from the LSC/interconnect and the LSC/ASM interfaces and AES analysis on a representative area. TEM and AES results represent the bulk and surface compositions, respectively.

		Atom %			
		LSC Bulk (TEM)			LSC Surface (AES)
	TEM sample A (near the interconnect)		TEM sample B (near the anode)		
Element	Cr-rich region	Co-rich region	Cr-rich region	Co-rich region	Cr-rich region	Co-rich region
La	54.9	22.4	50.0	23.1	28.0	37.0
Sr	2.8	2.8	4.2	3.8	—	—
Co	15.5	63.6	12.5	57.6	44.6	56.5
Cr	27.0	10.2	33.3	15.4	27.4	6.4
Co/Cr	0.57	6.24	0.38	3.74	1.63	8.78
La/Cr	2.03	2.20	1.50	1.50	1.02	5.75

SOEC stacks are operated at atmospheric pressure, the local P_{O_2} in the anode and contact layer of the cells can be greater than 10^5 Pa due to the generation and evolution of O_2.[37] Such high P_{O_2} favors the stability of La_2CrO_6, as shown in Ref. 36, while the exact value of local P_{O_2} in the anode and LSC contact layer is not determined in this paper. Thus, the findings reported in Ref. 36 support that the secondary phases of lanthanum chromite and chromate formed were stable at the operating conditions of SOECs. This decomposition of the LSC perovskite structure leads to an adverse change in the electronic properties of the contact layer. Thus, the decomposition of the
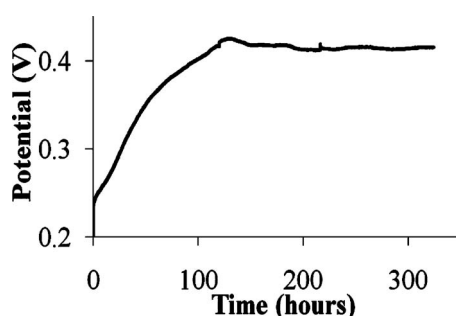
LSC perovskite into secondary, low conducting, and less active phases can be a chief cause for the SOEC performance degradation.

The chemistry and microstructure of the surface of LSC grains significantly varied throughout the LSC cross section, as was shown by AES results. Figure 4 shows that significant differences in the local compositions and chemical signature at the surface of LSC grains existed even within a micrometer scale. The ratio of La to Co experienced a drastic departure from its stoichiometric value of 0.8 and varied from 0.65–9.50 (for the data shown in Fig. 4) and 0.65–16.65 overall. The lack of Sr and only weak presense of Co in the cross section of LSC accompanied by Sr- and Co-enriched regions on the top of LSC (Fig. 5) indicate that, in particular, the Sr and Co
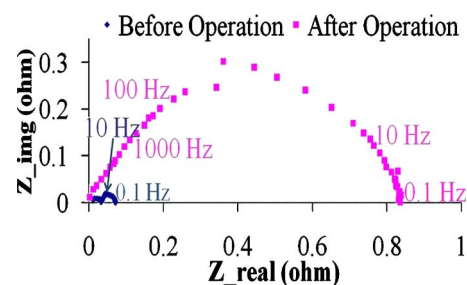

Figure 7. Cell performance and overpotential as a function of time for the half-cell REF#1. Under a constant current density of 0.4 A/cm² at 816°C in air, the potential difference across the cell increased with time and stabilized after about 120 h.

Figure 8. (Color online) Electrochemical impedance as Nyquist plot for the anode of REF#1 before and after its operation. The impedance of the electrode increases from 0.07 to 0.83 Ω over the test period, indicating degradation on the "electrolytic" electrode (anode) of the cell.
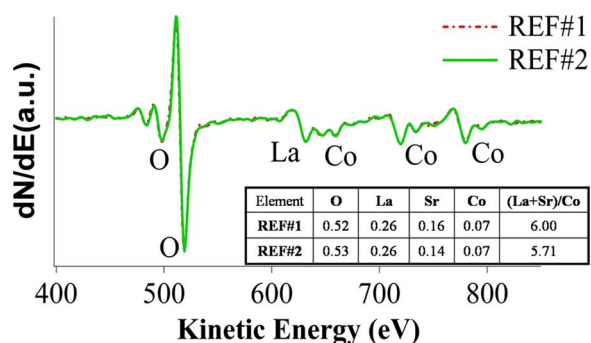
Figure 9. (Color online) Comparison of AES spectra from an area in each of the LSC cross-sectional surface of cells REF#1 and REF#2.
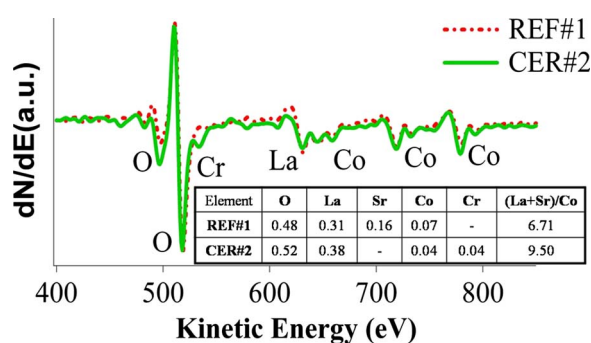

Figure 10. (Color online) Comparison of the AES data from an area in each of the LSC cross section of cell REF#1 with that of cell CER#2.

cations migrated from the contact layer structure to the LSC/interconnect interface. This indicates a long-range (over ∼20 μm) transport and an inhomogeneous segregation of the A- and B-site cations from the LSC layer, consequently leading to the dissociation of the perovskite LSC phase in the contact layer. The directions of the cations and charge carriers involved across the SOEC are schematically shown in Fig. 11.

Complementary to the surface-sensitive AES results, the bulk-sensitive TEM/EDX results showed that the Cr content in LSC varied at 10–33%, larger than at the LSC surface, indicating different mechanisms of Cr reaction at LSC surface vs bulk. Results for Sr were consistent with those from AES: a maximum of only 4% found in the bulk of LSC and below the detection limit on the surface. The results from TEM/EDX confirm the severe dissociation of LSC and show that the secondary phase formation was on the nanoscale (Fig. 6). The nanoscale Cr-rich regions were associated with enrichment of La and depletion of Co, indicating a new phase between Cr and La. The La/Cr ratio of 2 in the LSC/interconnect interface region indicates the presence of La_2CrO_6. The drop of the La/Cr ratio to 1.5 near the anode suggests the formation of different chemical phases
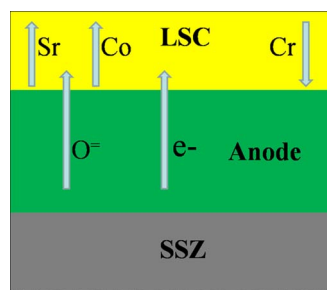

Figure 11. (Color online) Schematic for the transport of cations and charge carriers across the SOEC.

near the LSC/interconnect and LSC/ASM interfaces in the contact layer. An increase in the Cr content (relative to La) near the anode could suggest the presence of $LaCrO_3$ and/or Cr_2O_3 near the anode. Co-containing phase is likely to be Co_3O_4. This is consistent with the Raman spectroscopy results indicating their presence at the top of the contact layer upon long-term testing.

Upon these observations, we hypothesize that the long-range transport of Sr and Co can be driven by two primary mechanisms: (*i*) Cr-related thermodynamics, where the Cr-containing species (in the vicinity of the interconnect) could thermodynamically favor the presence of select cations (i.e., Sr and Co) at the region interfacing the interconnect and (*ii*) the electronic or oxygen ion current carrying the cations along the same direction. To test these hypotheses and isolate the actual mechanism(s) for severe cation segregation and phase separation in the LSC contact layer, REF#1 was operated in controlled electrochemical environments. The increase in potential difference across the reference cell shown in Fig. 7 indicated that cell REF#1 degraded with time even in the absence of Cr-containing interconnects or other possible Cr species in the testing environment. The cell potential doubled (from 0.23 to 0.42 V) within 5 days before eventually stabilizing. Nyquist plot on the anode of REF#1 in Fig. 8 shows that the impedance of the anode increased by 0.76 Ω during its operation. The significant degradation observed in this experiment suggests that there exists at least one other mechanism that contributes to the degradation even in the absence of Cr poisoning in this particular experiment. Figure 9 suggests that there was no significant difference in the chemical compositions and microstructure of the LSC contact layer of the heat-treated cells without electrochemistry (REF#2) and the cells that were operated under a constant current density (REF#1). The A-site to B-site cation ratio for the contact layer of REF#1 and REF#2 varied from 5.71 to 6.71. Even though the contact layer composition for REF#1 and REF#2 was uniform, it was A-site enriched. However, for CER#2, the dissociation of LSC across its cross section was drastically nonuniform, with A-site to B-site cation ratio for CER#2 varying from 0.65 to 16.65. Thus, cation segregation in CER#2 was far more severe than in REF#1 and REF#2. Furthermore, as evident in Fig. 10, REF#1 has considerable Sr and Co content on the LSC cross-sectional surface, while the cross section of CER#2 was depleted in Sr and Co cations even though both the REF#1 constant current density and the CER#2 initial current density were the same (0.4 A/cm²). Hence, electronic or ionic current alone cannot be the dominating factor in the long-range migration of Sr and Co in CER#2 from the long-term stack tests. The presence of Cr (in the stainless steel interconnect) in the vicinity of the LSC layer and the corresponding thermodynamic driving forces must be a major cause for the long-range transport of cations to the top of the LSC layer and the consequent nonuniform dissociation of the LSC perovskite phase. Thus, we suggest that the formation of the poorly conducting secondary phases is due to the LSC dissociation driven by the La–Cr–O related thermodynamics under the electrolytic potential and atmosphere at the anode. This result is consistent with the observations of Jiang et al. and Quadakkers et al.[17] that the oxygen electrode (or the contact layer here) could dissociate into secondary phases driven by Cr-related thermodynamics, and Cr-poisoning is not solely an electrochemically driven process. Such dissociation of the LSC contact layer into less conducting phases is the dominant cause for the degradation of the anode performance for the SOECs investigated here.

Based on the results from the Raman spectroscopy, AES, TEM, and electrochemical measurements in this research, we suggest the following mechanism as a likely path for the Cr-related degradation of the LSC contact layer. The process can be initiated by the volatilization of Cr to Cr⁺⁶-containing species, CrO_3 or $CrO_2(OH)$, at the interconnect, a process already suggested for SOFCs.[13] A set of reactions between the CrO_3 or $CrO_2(OH)$ species and the LSC surface phase/species, serving as nucleation agents, initiates the formation of secondary phases with low conductivity. The La–O and Sr–O segregates at the surface of LSC grains are the likely nucleation
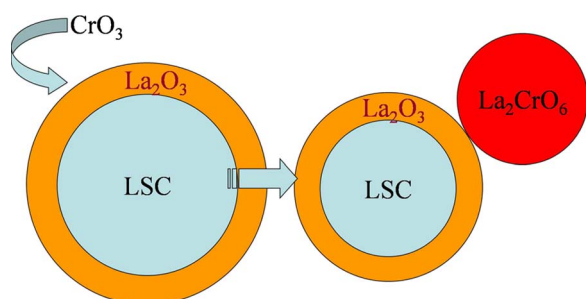
Figure 12. (Color online) Schematic of a possible reaction mechanism between Cr species and the LSC surface phases. The surface of the LSC grains is A-site segregated in the as-prepared condition. These A-site-enriched phases on the surface react with the Cr-containing species and form La_2CrO_6.

agents in the latter theory. In this investigation, a clear enrichment in La and Sr on the surface of both the as-prepared and the tested reference half-cell LSC layer grains were found by AES. Consistent with Zhen et al.[18] and Chen et al.'s[19] theory, we hypothesize that this surface segregation of A-site species enhances the Cr deposition. Thus, the La-enriched La–O phase on the surface of LSC grains likely reacts with the CrO_3 species, leading to the formation of the $LaCrO_3$ or La_2CrO_6 phases observed in the Raman spectroscopy and STEM/EDX studies here. The proposed scheme governing the aforementioned reaction is shown in Eq. 1, following the notation used by Zhen et al.[18] While a possible reaction scheme is depicted in Fig. 12, the exact mechanism by which Cr drives such long-range transport of cations leading to La–Cr phase formations and the relation of this process to the electrochemical potential and gas pressure conditions in SOEC anode should be further quantified in terms of the thermodynamics involved in these reactions

$$Cr_2O_3 \rightarrow CrO_3(g)$$

$$CrO_3(g) + N \rightarrow Cr\text{–}N\text{–}O_x$$

$$CrO_3(g) + La_2O_3 \rightarrow La_2CrO_6 \qquad [1]$$
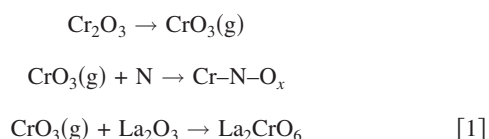
where N is the nucleation agent, here, a La-containing species, e.g., La_2O_3.

Conclusions

The degradation mechanism of LSC as the contact layer of SOEC anodes, particularly in the context of Cr poisoning, was investigated here. The key observations obtained in this work are the following:

1. Raman spectroscopy at the LSC/interconnect interface showed that the LSC contact layer had at least partially dissociated, and the poorly conducting secondary phases of Co_3O_4, Cr_2O_3, $LaCrO_3$, and La_2CrO_6 were formed. These observations indicated that Cr transported from the stainless steel interconnects into the LSC layer, leading to electronic de-activation of the contact-layer.

2. AES results showed that the as-prepared surface chemistry of LSC showed a spatially uniform A-site (La and Sr) enrichment. In the tested SOEC stack cells, an average of 7% Cr on the cross-sectional surface of the LSC layer was found. The La/Co ratio showed a severe and nonuniform dissociation of the contact layer. Long-range transport of the Sr and Co cations to the top of the contact layer particularly prevailed with no detectable Sr remaining in the bulk of the layer. The top of the contact layer (LSC/interconnect interface) was decorated by Co-rich crystallites, possibly Co–Cr oxides, and a Sr-rich surface layer. This process could be associated with cation segregation and phase separation under the electrolytic potential and electronic and ionic current conditions and/or the presence of Cr species driving reactions to dissociate LSC.

3. STEM analysis confirmed the dissociation of the LSC contact layer due to the formation of secondary phases separated at the nanoscale. The bulk had a larger Cr content (10–33%) than the surface of the layer grains, indicating different composition profiles for Cr reactions in the bulk and at the surface. Cr and La coexisted in phase-separated regions, identified as either $LaCrO_3$ or La_2CrO_6 in the bulk of the layer. Consistent with the AES results from the surface, Sr signal was absent from the bulk, indicating the complete separation of Sr from the bulk contact layer microstructure and microchemistry.

4. EIS and AES analysis on the reference half-cells operated in controlled electrochemical environments in air showed that the cells degraded even in the absence of Cr in the system. However, the microstructure and surface composition of the LSC contact layer were stable and uniform throughout, although largely A-site enriched, with clear presence of Sr in the structure. These observations show that the LSC contact layer stayed stable under electrolytic (anodic) conditions when not subjected to Cr-containing species.

We conclude that the formation of poorly conducting secondary phases due to the dissociation of the LSC contact layer leads to the deterioration of the electronic activation of the anode and thus contributes to the significant degradation of the SOEC performance. Our results indicate that the dominant cause for the LSC dissociation is the inward transport of the Cr-containing phases from the stainless steel interconnects into the contact layer microstructure and is driven by the thermodynamics governing (La and Sr) Cr–O phases under electrolytic polarization and oxygen partial pressure conditions. The results suggest a mechanism for Cr deposition, which can nucleate between the volatile Cr-containing species [CrO_3 or $CrO_2(OH)$] and the La–O and Sr–O segregates on the initial LSC surface, initiating the formation of secondary phases. The exact mechanism by which Cr causes such long-range transport of Sr and Co cations and the consequent La–Cr–O phase formations and the relation of this process to the electrochemical potential and gas pressure conditions in SOEC anode should be further quantified in terms of the thermodynamics involved in these reactions.

References

1. B. Yildiz, K. J. Hohnholt, and M. S. Kazimi, *Nucl. Technol.*, **155**, 1 (2006).
2. B. Yildiz and M. S. Kazimi, *Int. J. Hydrogen Energy*, **31**, 77 (2006).
3. M. S. Sohal, J. E. O'Brien, C. M. Stoots, J. S. Herring, J. Hartvigsen, D. Larsen, S. Elangovan, J. D. Carter, V. I. Sharma, and B. Yildiz, Report no. INL/EXT-09-16004, Report to the U.S. Department of Energy by Idaho National Laboratory (2009).
4. J. Hartvigsen, S. Elangovan, C. M. Stoots, J. E. O'Brien, and J. S. Herring, Paper 173733 presented at ANS Embedded Topical: International Topical Meeting on the Safety and Technology of Nuclear Hydrogen Production, Control, and Management, Boston, MA, June 24–28, 2007.
5. *High Temperature Solid Oxide Fuel Cells: Fundamentals, Design, and Applications*, S. C. Singhal and K. Kendell, Editors, p. 134, Elsevier, New York (2003).
6. J. E. O'Brien, C. M. Stoots, J. S. Herring, and J. J. Hartvigsen, *Nucl. Technol.*, **158**, 118 (2007).
7. B. Borglum, in *The 10th Annual Solid State Energy Conversion Alliance (SECA) Workshop*, SECA (2009).
8. A. Hauch, S. D. Ebbesen, S. H. Jensen, and M. Mogensen, *J. Electrochem. Soc.*, **155**, B1184 (2008).
9. J. R. Mawdsley, J. D. Carter, A. J. Kropf, B. Yildiz, and V. A. Maroni, *Int. J. Hydrogen Energy*, **34**, 4198 (2009).
10. Y. Matsuzaki and I. Yasuda, *J. Electrochem. Soc.*, **148**, A126 (2001).
11. Y. Matsuzaki and I. Yasuda, *Solid State Ionics*, **132**, 271 (2000).
12. J. W. Fergus, *Int. J. Hydrogen Energy*, **32**, 3664 (2007).

13. M. Stanislowski, E. Wessel, K. Hilpert, T. Markus, and L. Singheiser, *J. Electrochem. Soc.*, **154**, A295 (2007).
14. M. Stanislowski, J. Froitzheim, L. Niewolak, W. J. Quadakkers, K. Hilpert, T. Markus, and L. Singheiser, *J. Power Sources*, **164**, 578 (2007).
15. E. Konysheva, H. Penkalla, E. Wessel, J. Mertens, U. Seeling, L. Singheiser, and K. Hilpert, *J. Electrochem. Soc.*, **153**, A765 (2006).
16. K. Hilpert, D. Das, M. Miller, D. H. Peck, and R. Weiß, *J. Electrochem. Soc.*, **143**, 3642 (1996).
17. W. J. Quadakkers, H. Greiner, M. Hansel, A. Pattanaik, A. S. Khanna, and W. Mallner, *Solid State Ionics*, **91**, 55 (1996).
18. Y. Zhen, A. I. Y. Tok, F. Y. C. Boey, and S. P. Jiang, *Electrochem. Solid-State Lett.*, **11**, B42 (2008).
19. X. Chen, L. Zhang, and S. P. Jiang, *J. Electrochem. Soc.*, **155**, B1093 (2008).
20. S. P. Jiang, J. P. Zhang, L. Apateanu, and K. Foger, *J. Electrochem. Soc.*, **147**, 4013 (2000).
21. Z. Yang, G. Xia, P. Singh, and J. W. Stevenson, *J. Power Sources*, **155**, 246 (2006).
22. T. Kawada, N. Sakai, H. Yokokawa, and M. Dokiya, *Solid State Ionics*, **50**, 189 (1992).
23. H. Taimatsu, K. Wada, H. Kaneko, and H. Yamamora, *J. Am. Ceram. Soc.*, **75**, 401 (1992).
24. A. Grosjean, O. Sanseau, V. Radmilovic, and A. Thorel, *Solid State Ionics*, **177**, 1977 (2006).
25. S. P. Simner, M. D. Anderson, M. H. Engelhard, and J. W. Stevenson, *Electrochem. Solid-State Lett.*, **9**, A478 (2006).
26. N. Colthup, S. E. Wiberley, and L. H. Daly, *Introduction to Infrared and Raman Spectroscopy*, 3rd ed., p. 60, Academic, New York (1975).
27. H. Y. Chen and F. H. Lu, *Thin Solid Films*, **515**, 2179 (2006).
28. Y. Raitses, C. H. Skinner, F. Jiang, and T. S. Duffy, *J. Nucl. Mater.*, **375**, 365

29. M. Li, Z. Feng, P. Ying, Q. Xin, and C. Li, *Phys. Chem. Chem. Phys.*, **5**, 5326 (2003).
30. M. N. Iliev, A. P. Litvinchuk, V. G. Hadjiev, Y. Q. Wang, J. Cmaidalka, R. L. Meng, and Y. Y. Sun, *Phys. Rev. B*, **74**, 214301 (2006).
31. D. L. Hoang, A. Dittmar, J. Radnik, K. W. Brzezinka, and K. Witke, *Appl. Catal., A*, **239**, 95 (2003).
32. N. Orlovskaya, D. Steinmetz, S. Yarmolenko, D. Pai, J. Sankar, and J. Goodenough, *Phys. Rev. B*, **72**, 014122 (2005).
33. X. P. Shen, H. J. Miao, H. Zhao, and Z. Xu, *Appl. Phys. A: Mater. Sci. Process.*, **91**, 47 (2008).
34. I. F. Ferguson, *Auger Microprobe Analysis*, p. 16, Hilger, New York (1989).
35. D. B. Williams and C. B. Carter, *Transmission Electron Microscopy*, Springer, New York (1996).
36. E. Povoden, M. Chen, A. N. Grundy, T. Ivas, and L. J. Gauckler, *J. Phase Equilib. Diffus.*, **30**, 12 (2009).
37. J. Hartvigsen, Ceramatec Inc., Personal communication.
38. P. Hjalmarsson, M. Soggard, A. Hagen, and M. Mogensen, *Solid State Ionics*, **179**, 636 (2008).
39. D. S. Tsvetkov, A. I. Vylkov, A. Y. Zuev, and A. N. Petrov, *Russ. J. Phys. Chem.*, **82**, 855 (2008).
40. S. Elangovan, Ceramatec Inc., Personal communication.
41. S. Sakamoto, M. Yoshinaka, K. Hirato, and O. Yamaguchi, *J. Am. Ceram. Soc.*, **80**, 267 (1997).
42. A. Atkinson, M. R. Levy, S. Roche, and R. A. Rudkin, *Solid State Ionics*, **177**, 1767 (2006).
43. K. P. Ong, P. Wu, L. Liu, and S. P. Jiang, *Appl. Phys. Lett.*, **90**, 044109 (2007).

(2008).